Heat transfer, fluid flow and electromagnetic model of droplets generation and melt pool behaviour for wire arc additive manufacturing

S. Cadiou, M. Courtois, M. Carin, W. Berckmans, P. Le Masson

HEAT TRANSFER, FLUID FLOW AND ELECTROMAGNETIC MODEL OF DROPLETS GENERATION AND MELT POOL BEHAVIOUR FOR WIRE ARC ADDITIVE MANUFACTURING

S. CADIOU*, M. COURTOIS*, M. CARIN*, W. BERCKMANS*, P. LE MASSON*
Univ. Bretagne Sud, UMR CNRS 6027, IRDL, F-56100 Lorient, France, e-mail: mickael.courtois@univ-ubs.fr

Abstract:
In this study, a numerical model of Wire Arc Additive Manufacturing has been developed to obtain the geometry of the part as well as its temperature field from the operating parameters. This predictive model takes into account electromagnetism, fluid flow and heat transfer in the arc and the melt pool. The Lorentz forces, shear stress, arc pressure, and Joule effect are calculated. This model is developed using the COMSOL Multiphysics® software. In order to simulate the addition of layer-by-layer material and the strong topological changes, the level set interface tracking method is used. This model aims to simulate the build-up of a 304 stainless steel rod starting from the operating parameters in the case of a pulsed currents. The detachment of droplets of the deposited metal and their fall along the vertical axis are modelled to predict the geometry and the thermal history of the workpiece. The "material supply / cooling" cycles between each layer are simulated. To validate this model, the geometry and the temperature field are analysed and compared to experimental data.

Keywords : additive manufacturing; arc-wire, droplets; melt pool; pulsed current; numerical modelling; level set method; magnetohydrodynamics; heat transfer.

1. Introduction

The additive manufacturing (AM) of metal parts is a revolutionary process with strong potential. A large number of additive manufacturing methods are now available. The current work focuses on the Wire Arc Additive Manufacturing (WAAM), which is a highly promising process due to its high deposition rate, significant raw material savings, the ability to manufacture large components and significant cost savings [1-3]. This process uses an electric arc as a heat source and a wire as deposited material and is very similar to the GMA (Gas Metal Arc) welding process. The WAAM process can be very suitable for designing large structures. However, for such dimensions, the traditional trial-and-error methodology used to identify satisfying operating parameters becomes very expansive. Modelling and simulation can help both from a thorough understanding of the physical phenomena and the definition of optimal conditions to produce defect-free and reliable AM parts. Numerical simulation provides an efficient way to understand the influence of the operating parameters on the geometry, the thermal cycles, the microstructure, the distortions and the residual stresses observed in the AM parts.

However, there are very limited numerical studies in 3D to simulate multilayer deposition such as in WAAM processes, since a complete 3D modelling has to face prohibitive calculation times. In order to reduce computation times, these models are generally simplified and based on empirical laws requiring a calibration of input parameters with experimental data. The droplet formation and detachment, droplet flight in arc plasma and impingement of droplets are not explicitly simulated. Bai [4] developed a 3D model to investigate the fluid flow and heat transfer behaviours in multilayer deposition of plasma arc welding (PAW). A VOF method is used to track the melt pool surface. The mass feeding process is modelled as a source term in the mass conservation equation. The location of the mass input is determined according to experimental data. The modelling of the heating arising from the interaction with the arc is also simplified using a modified double-ellipsoidal volumetric heat source model based on calibrated parameters with infraredimaging. This model is used to simulate the 1st, 2nd and 21st layer depositions. However, due to prohibitive computation time, the simulation of the 21st layer is initialized with the experimental profile of

the 20th layer. Hejripour [5] used an Arbitary Lagrangian-Eulerian (ALE) method to predict the shape of the first layer in a WAAM process. Gaussian functions are chosen to describe the heat input, the current density and the arc pressure. The profile of the free surface is calculated by minimizing the total potential energy of the surface resulting from a balance condition between surface tension, hydrostatic pressure and arc pressure. However, this method is difficult to apply for multilayer deposition. Furthermore, several computations were required in order to find the values of the Gaussian functions that give the best match between numerical and experimental weld zone profiles. In order to avoid this tedious calibration, there is a need to develop multiphysics model describing all the physical phenomena in the arc with the detachment of droplets and their transfer into the melt pool.

In the literature, such works have focused on models simulating Gas Metal Arc Welding (GMAW) rather than Wire Arc Additive Manufacturing (WAAM).

Jones and al. [6] developed a model of droplet detachment under the influence of electromagnetic forces. In their model, electromagnetic forces are calculated from the geometry of the droplet, and are applied to the centre of gravity of the droplet. Their model deals with the three main steps of the GMAW process:

- the growth of droplet,
- its detachment from the wire tip,
- the transfer of the droplet through the arc plasma.

Two types of current were studied, a direct current and a pulsed current. For both currents, the authors had to reduce the value of the surface tension in order to reproduce a droplet detachment consistent with experimental observations. This adjustment was found necessary by the authors since their model does not take into account the radial component of the magnetic force.

In a companion paper, the same authors [7] analysed the evolution of the magnetic forces during the detachment of the droplets. They pointed out that the magnetic force depends only on the shape of the droplet and the current path and not on the internal fluid flow in the droplet. In their approach, the shape profiles of droplets are determined with experimental measurements and are used to compute the magnetic forces.

Fan and Kovacevic [8] developed a unified 2D axisymmetric model to simulate all the steps of the GMAW welding process. Their model predicts the formation of the droplets, their detachment, as well as their impingement into the melt pool. The coupled equations governing the conservation of mass, momentum, energy plus Maxwell's equations are solved in the electrode, the arc and the weld pool. A Volume of Fluid (VOF) method is employed to track the moving free surface. A direct current of 160A is considered, leading to a globular regime, where the droplet diameter is larger than the wire diameter. The arc composed of ionized argon gas is supposed to be in local thermodynamic equilibrium (LTE). The flows in gas and liquid are assumed to be laminar. The heating of the droplet in the plasma is neglected, compensated by the vaporization of the droplet surface. To validate their model, they compared numerical results with fast-speed imaging measurements, combined with a laser backlighted shadowgraphic method.

Hu and Tsai [6,7] proposed a similar model to simulate the dynamic welding process in the electrode, the arc and the weld pool for a constant current of 200A. Their calculations show how the moving droplets and the deformed melt pool affect the current, temperature, velocity and pressure distributions in the arc column. Their findings put into question the traditional assumption of a Gaussian distributions for arc pressure, current, and heat flux at the melt pool surface.

Murphy [11] developed a different approach to model a GMAW process with a three-dimensional model. An equilibrium surface method is used to track the free surface of the melt pool instead of the VOF method. The influence of the droplets on the arc and the weld pool is taken into account through source terms obtained with time-averaged integration. This approach greatly reduces the calculation time allowing the use of large time steps. The calculated depth and shape of the weld pool were in good agreement with cross-section macrographs.

Ogino and Hirata [12] proposed a 3D model including the interactions between droplets and arc plasma. They developed a decoupled model, where the arc plasma and the droplet are calculated as two distinct fluids. At a given time step, the characteristics of the arc plasma, such as temperature, velocity and pressure fields, are calculated first, for a fixed droplet shape. Then, the metal transfer phenomena are calculated using the characteristics of the arc plasma as boundary conditions. At the next time step, the arc plasma is calculated using the new droplet shape as the boundary condition. The VOF method is used to track the new shape of the droplets. These calculations are carried out for different currents in order to analyse the transition from globular to spray transfer. The calculated droplet transfer frequencies were in good agreement with experimental data. They found that at low currents, surface tension is the main factor responsible for the transfer mode, but electromagnetic force becomes dominant at high currents.

In [13], Ogino et al. showed that the transition from globular to spray is also influenced by the shielding gas. By comparing their calculations obtained with argon and an argon-CO_2 mixture, they found that the nature of the gas has an impact on the detachment frequency and temperature of the droplets. In [14], they investigated the influence of trapezoidal pulse current in pulsed MIG welding. Their computations showed that a periodic behaviour is observed for the droplet but also for the arc plasma and the metal vapor. The influence of the properties of the filler wire material, such as surface tension and viscosity, on the behaviour of droplets are also studied numerically. They highlighted that for a low surface tension coefficient, there will be more droplets to detach for a given pulse duration. The same observation is made with the dynamic viscosity of the filler wire. They did not validate their model through experiments.

Other authors, such as Zhao and Chung [15], developed a coupled magnetothermal-hydrodynamic model to study metal transfer and heat transfer behaviour in the GMAW process using an alternative current. They used the level set method to track the moving interface. First, the effect of the electrode polarity on the arc properties is studied. They also studied the behaviour of the droplets in terms of size, shape and temperature for direct and alternating current. In addition, a quantitative analysis of heat fluxes in the electrode is also performed to explain the thermal mechanism of the droplet transfer differences between a direct and alternating current. To validate their model, the simulated results are then compared to high-speed images at different times during the welding cycle. Their model does not simulate the melt pool. In [16], these authors investigated the transition from globular to spray mode with a similar model but using a phase field method to track the liquid-gas interface. The influence of driving forces in the different transfer modes is studied. Moreover, they found that the phase field method predicts more realistic droplet diameter as a function of current, compared with VOF method, due to a better estimation of the current path between the droplet crossing and the arc plasma. However, their model does not simulate the melt pool and its interaction with the droplets. In [17], the same authors investigated the influence of different types of current waveforms on the dynamic droplet transfer behaviour and compared the numerical results with experimental data obtained from high-speed camera for an exponential current waveform type. It is found that the current waveforms strongly alter the detaching moment and the droplet velocity, but the heat fluxes into the electrode wire are not significantly affected. As in [11-12], the melt pool is not modelled.

In this paper, we propose a 2D axisymmetric model to simulate a pulsed WAAM process. This model not only describes the formation of the droplet at the electrode tip, its detachment and its flight through the arc plasma, but it also predicts its impingement into the melt pool, the growth of the melt pool and the formation of the deposited bead. It is based on the computation of magnetothermal-hydrodynamic equations in all domains (wire, arc, melt pool, substrate) with the level set method for the interface tracking. This model is used to simulate the building of a vertical rod in the case of a pulsed current. This current presents a periodic signal with a peak value at a given frequency inducing the detachment of a droplet. This model requires only the knowledge of the operating parameters without any assumption on the arc distribution, to predict the temperature field in the part during the multi-layered deposition as well as its geometry. However, in order to reduce the computation time during

the multi-layered deposition, some simplifications are made. The numerical results are compared to experimental data giving the shape of the geometry of the solidified bead and fusion zone and as well as temperature measurements. All the numerical developments are made using COMSOL Multiphysics® software version 5.4.

2. Modelling of the building of the rod

The mathematical modelling of such a process involves different physics like heat transfer, fluid flow, or electromagnetism. The present model is focused on these three physics, which is also refer to a Magneto-Hydro Dynamics (MHD) model. The aim of this approach is to predict the heat transfer and fluid flow in both the arc plasma and the weld pool.

2.1. Assumptions

Considering the complexity of multiphysics coupling (electromagnetic, thermal and fluid flow), assumptions have been made to reduce the difficulty of modelling. These assumptions are commonly used [12-14] and are listed below:

- The model is solved in 2D axisymmetric, since the torch is static.
- The plasma is in local thermodynamic equilibrium (LTE). This assumption means that species such as ions, neutrons are supposed to have the same temperature.
- The fluid flow in the plasma and melt pool are considered to be Newtonian laminar with an incompressible approach.
- Thermal dependence of the surface tension coefficient known as Marangoni effect is neglected because of the dispersion of values in literature (dependence of the exact chemical composition). Moreover, the Marangoni effect is believed not to be the predominant driven force here, since the falling of the numerous droplets in the melt pool causes a strong fluid flow.
- Buoyancy force is taken into account using the Boussinesq approximation.
- The effect of metal vapors coming from the vaporisation at the melt pool surface is not included in the model.

Metal vapors are not taken into account in the model as in Zhao's model [15]. However, this phenomenon is more detailed for TIG welding. When the arc interacts with the anode, metal vapor can be generated if the surface temperature reaches the evaporation point. Several studies have been carried out on the understanding of the influence of these metallic vapors. Lago, [18], shows through his numerical model that metal vapors tend to cool the plasma essentially at the edges. Current densities, in the presence of metal vapors, increase at the centre of the arc and decrease at the edges. Moreover, the vapors increase the current densities at the anode. The greater flux comes from the increase of the electrical flux due to the electrical conductivity increase. These remarks are consistent with Mougenot [19]. Murphy and Tanaka et al [20] have shown that the maximum value of the current density is slightly lower (5.5% difference) when the metal vapors are taken into account. In our case, we chose to neglect the metallic vapors since their effect is rather small but also in order to simplify the calculations.

In order to simulate the material addition, the level set model is chosen to track the gas-metal interface.

2.2. Presentation of the level set method

A multiphase formulation is used to describe the interaction between the arc plasma and the liquid metal. The arc plasma is considered as gaseous phase. The domains of the wire and the substrate and the molten metal are treated as liquid phase. The level set method is

used to describe the dynamic shape of the interface liquid-gas in order to study the melting of the electrode, the detachment of droplets from the electrode tip, their transfer through the arc plasma, the impingement of droplets into the melt pool and the solidification of the deposition after the arc extinguishing.

The level set method [21] consists in defining a ϕ variable on a fixed Cartesian grid to represent the interface between gas and metal. This variable ϕ is arbitrary defined to 0 in gas, and 1 in metal. At the vicinity of the gas/metal interface, this variable varies continuously using a smoothed step function. However, the thickness of this transition must be small enough to represent the interface accurately but not too small, in order to avoid numerical divergence. The location of the interface gas-metal is then determined by simply locating the variable $\phi = 0.5$.

This variable also serves for defining the appropriate properties in each material (gas or metal). So, for example, the density is defined as follows:

$$\rho = \rho_{gas} + (\rho_{steel} - \rho_{gas})\phi \qquad (1)$$

where ρ_{gas} represents the gas density and ρ_{steel} the metal density. These properties can be temperature-dependant. Note that, at the interface, a mean value for the material properties is set.

The displacement of the interface is obtained by solving a transport equation related to the solution velocity field, expressed as follows [22]:

$$\frac{\partial \phi}{\partial t} + \vec{v}.\overrightarrow{grad}(\phi) = \gamma_{ls}\,\overrightarrow{div}\left(\varepsilon_{ls}\,\overrightarrow{grad}(\phi) - \phi(1-\phi)\frac{\overrightarrow{grad}(\phi)}{|\overrightarrow{grad}(\phi)|}\right) \qquad (2)$$

where γ_{ls} is a reinitialization speed (m/s) and ε_{ls} is the interface thickness controlling parameter (m). The left hand-side of the equation represents the classical terms for a transport equation. The evolution of the field ϕ will change according to the fluid velocity. The right hand-side allows the reinitialization of the level set function to avoid numerical instability [22-24]. This term ensures that the gradient of ϕ at any given point of a level set does not change dramatically over time. Indeed, if the gradient of the level set function becomes too small on the interface, the location of the interface becomes sensitive to perturbation. If the gradient is too large with respect to the mesh, the representation of the interface will not be accurate. So, in order to keep the thickness of the interface constant, and obtain a stabilized motion of the interface, the value of the reinitialization speed is here chosen to be of the same order of magnitude as the velocity field. The parameter ε_{ls} determines the thickness of the region where the variable ϕ varies smoothly from zero to one. Its value is chosen here in order to have at least three elements in this region.

Moreover, the ϕ variable can be derived spatially to define a Dirac delta function $\delta(\phi)$. This function is approximated by a smooth function according to $\delta(\phi) = 6\,|\overrightarrow{grad}(\phi)|\,|\phi\,(1-\phi)|$, which is non-zero only near the gas-metal interface. This function makes it possible to apply all the existing interfacial boundary conditions between the two fluids through volume source terms introduced into the conservation equations in the computational domain.

2.3. Electromagnetism

In order to calculate the electromagnetic forces acting on the liquid and gas phases and the Joule heating, the Maxwell equations are solved.

$$div\left(\sigma_e\overrightarrow{grad}(V) + \sigma_e\,\frac{\partial \vec{A}}{\partial t}\right) = 0 \qquad (3)$$

$$\sigma_e \frac{\partial \vec{A}}{\partial t} + \frac{1}{\mu_0} \overrightarrow{rot}\left(\overrightarrow{rot}(\vec{A})\right) + \sigma_e \overrightarrow{grad}(V) = \vec{0}$$

where σ_e is the electrical conductivity, V is the electrical potential, μ_0 is the magnetic permeability and $\vec{A}$ is the magnetic vector potential.

2.4. Conservation of energy

The differential equation governing the energy conservation is given below:

$$\rho C_p^{eq} \left(\frac{\partial T}{\partial t} + \vec{v}.\overrightarrow{grad}(T) \right) = div\left(\bar{\bar{k}}\, \overrightarrow{grad}(T)\right) + S_v \qquad (4)$$

where ρ is the density, C_p^{eq} is an equivalent specific heat, that equals Cp in the arc-plasma domain, and is modified to $C_p + L_f \frac{df_L}{dT}$ in the metal domain to account for the latent heat of fusion L_f, k is the thermal conductivity, T is the temperature, and S_v is a volumetric heat source term described below:

$$S_v = S_{Joule\ effect} + S_{rad} + S_{cathode/plasma\ interface} + S_{anode/plasma\ interface} + S_{level\ set} \qquad (5)$$

Each term of this equation is detailed hereafter:

- *Joule effect*

After arc initiation, the argon is partially ionized making it a conductor of electric current. The flow of the electric current between the wire and the melt pool generates a strong heating. This phenomena is called Joule heating effect, also known as Ohmic heating, This effect, which represents the main energy input in the plasma, is modelled by a volumetric heat source added in the energy equation. This heat source is therefore present in gas and steel, both having an electric current going through. The Joule effect is determined by solving the electromagnetic equations, and corresponds to the following equation:

$$S_{Joule\ effect} = \vec{j}.\vec{E} \qquad (6)$$

where $\vec{j}$ is the current density calculated with the relation $\vec{j} = \sigma_e \vec{E}$ and $\vec{E}$ is the electric field calculated with the relation $\vec{E} = -\overrightarrow{grad}(V) - \frac{\partial \vec{A}}{\partial t}$. The variables V and $\vec{A}$ are directly calculated from electromagnetic equations.

- *Radiation of the plasma*

The term S_{rad} represents the radiation losses in the plasma. These losses are particularly difficult to calculate with the radiative transfer equation. So, as many authors [18–20], these losses are evaluated here using an approximate method based on a net emission coefficient, allowing reduced computation time. This coefficient results from the balance between the locally radiated power and its autoabsorption in the plasma. It depends on the temperature and the type of gas. The radiation losses are then calculated as follows:

$$S_{rad} = -4\pi\varepsilon_N \qquad (7)$$

where ε_N is the net emission coefficient of Argon taken from [28].

- *Cathode/plasma interface*

$$S_{cathode/plasma\ interface} = (j_i V_i - j_e \phi_c)\delta(\phi) \qquad (8)$$

At the cathode/plasma interface (the substrate surface), the emission of electrons is associated with a cooling effect represented by the term $j_e \phi_c$ where j_e is the electron current density at the surface of the cathode and ϕ_c the work function of the electrode wire [25]. This

current density cannot exceed the thermionic current density determined by the Richardson-Dushmann equation [25]

$$j_{em} = A_r T^2 \exp\left(-\frac{e\phi_e}{k_B T}\right) \quad (9)$$

where A_r is the Richardson's constant, T is the temperature, e is the elementary charge, ϕ_e is the cathode effective work function and k_B is the Boltzmann constant.

In addition, the cathode surface is heating by the absorption of positive ions. This heating is calculated by the ionization energy $j_i V_i$, where j_i is the ion current density and V_i the ionization potential of the gas. It is assumed that if the calculated current density is greater than the current density emitted by thermionic emission, the additional current density is then provided by the ions transferred from the plasma to the cathode. This ion current density is then expressed as follows [25]:

$$j_i = \begin{cases} j_c - j_{em} & if\ j_c - j_{em} > 0 \\ 0 & if\ not \end{cases} \quad (10)$$

As in [26], it is considered that the normal component of $\vec{j}$ at the surface is preponderant so it is stated: $j_c = |\vec{j}.\vec{n}|$.

- *Anode/plasma interface*

As for the plasma / cathode interface, additional energy terms modify the energy balance at the anode surface. Here, the anode is the wire. The heating induced by the absorption of electrons can be calculated by the expression $j_a \phi_a$, where ϕ_a is the anode work function and j_a the current density at the surface of the anode. Moreover, contrary to the energy balance of the plasma / cathode interface, the ion current density is assumed to be zero, therefore $j_a = j_e$. As before, we consider that $j_a = |\vec{j}.\vec{n}|$.

$$S_{anode/plasma\ interface} = (|\vec{j}.\vec{n}_a|\phi_a)\delta(\phi) \quad (11)$$

- *Level set adaptation*

$S_{level\ set}$ is an additional term to overcome some inherent drawbacks of the level set method. The transition of properties, both for the fluid flow problem and the thermal problem, leads to unrealistic effects. First, because the flows along the wire are distorted, convection is reduced accordingly. Secondly, thermal conductivity, specific heat, and density are modified at the wire surface, since they are in transition between the properties of steel and those of gas. Local heat balances are therefore also modified. With the level set method, at the beginning of the gas side surface, the thermal conductivity is increased by the transition allowing better heat diffusion in the domain and distorting the results. In addition, the final purpose is to melt the wire. The objective was therefore to find again a numerical trick to compensate for this defect due to the level set method, and thus to provide the necessary energy to melt the wire. To achieve this, the proposed solution is to add a heat source directly to the interface. This heat source applied to the wire is directly calculated from the heat source generated within the gas. The idea is to apply a Gaussian surface function to the end of the wire, whose power is the integral of the volume heat source calculated by the model. In the WAAM process, the plasma heat source is mainly located just below the tip of the filler wire. In the end, the power dissipated by the arc is therefore injected directly into the interface and is no longer advected from the gas to the wire surface, since the level set method does not allow the heat to be precisely transferred between the hot gas and the wire surface. To overcome this issue, a Gaussian heat source is introduced. The model via the Joule effect term directly calculates the power of this Gaussian. The Gaussian distribution parameter r_0 is taken equal to the radius of the electrode wire. The function ($az + b$) makes it possible to regulate the arc length in order to avoid short circuits, it is a spatial regulation. This function is unit-less. As the electrode tip gets closer to the substrate, this function

increases the energy at the tip of the wire and thus melts a larger amount of metal to induce the droplet detachment from the electrode tip to stabilize the arc length.

$$S_{level\ set} = \begin{cases} (az+b)\dfrac{e^{-\frac{r^2}{r_0^2}}}{\pi r_0^2}\displaystyle\int_V S_{Joule\ effect} dV\ \delta(\phi) & at\ the\ wire/plasma\ interface \\ \dfrac{e^{-\frac{r^2}{r_0^2}}}{\pi r_0^2}\displaystyle\int_V S_{Joule\ effect} dV\ \delta(\phi) & at\ the\ substrate/plasma\ interface \end{cases} \quad (12)$$

2.5. Conservations of mass and momentum

The fluid flows in the gas and the liquid metal are governed by the conservation of mass and momentum:

- Conservation of mass [9-18]

$$div(\vec{v}) = 0 \quad (13)$$

where $\vec{v}$ is the velocity vector.

- Conservation of momentum

$$\rho\left(\frac{\partial \vec{v}}{\partial t} + \overline{\overline{grad}}(\vec{v}).\vec{v}\right) = \overrightarrow{div}\left[-P\bar{\bar{1}} + \mu_f\left(\overline{\overline{grad}}(\vec{v}) + {}^t\overline{\overline{grad}}(\vec{v})\right)\right] + \overrightarrow{F_v} \quad (14)$$

where P is the pressure, $\bar{\bar{1}}$ the identity matrix, μ_f the dynamic viscosity and $\overrightarrow{F_v}$ the volume force expressed as follows:

$$\vec{F}_v = \vec{F}_{mag} + \vec{F}_{gravity} + \vec{F}_{surface\ tension} + \vec{F}_{Darcy} + \vec{F}_{friction} \quad (15)$$

- *Electromagnetic force:*

$$\vec{F}_{mag} = \vec{j} \times \vec{B}\left(1 + \frac{I_{max}}{I_{average}}\ freq_{current}\right) \quad (16)$$

where B is the magnetic flux density and j is the current density, $freq_{current}$ is a periodic time function ranging from 0 to 1 (equal to 1 when the maximum current is applied and equal to 0 when the low current is applied) to simulate the detachment of the droplet during the current pulse. As recalled, the current intensity is taken constant. However, in reality, there are pulses of intensity (Fig. 2) that allow the drop to be detached by acting on the electromagnetic forces. To take this increase into account, a $freq_{current}$ function (Fig. 7) has been added to increase these electromagnetic forces by taking the ratio of maximum intensity to average intensity.

- *Gravity*

$$\vec{F}_{gravity} = \rho\vec{g} \quad (17)$$

where ρ is the density and $\vec{g}$ is the acceleration due to gravity.

- *Surface tension*

$\vec{F}_{surface\ tension}$ represents a volume force taking into account the surface tension effect acting at the gas-metal interface. Indeed, with the level set method, all the interfacial forces are integrated in the momentum equation as body force by multiplying the surface force (in $N.m^{-2}$) by a Dirac delta function (δ in m^{-1}). For surface tension, this volume force is calculated according to [27]:

$$\vec{F}_{surface\ tension} = (\vec{n}\kappa + (I - \vec{n}.\vec{n}^T)\nabla)\gamma)\ \delta(\phi) \quad (18)$$

where κ is the curvature, γ is the surface tension coefficient.

- *Darcy*

$\vec{F}_{Darcy}$ represents an additional force to approximate the flow in the mushy zone as a porous media flow using a Darcy's law. With this term, the fluid flow becomes zero in the solid region of the electrode wire and the solid material.

$$\vec{F}_{Darcy} = -C\frac{(1-f_L)^2}{f_L^3+b}\vec{v} \tag{19}$$

where C is a relatively huge constant that ensures the decrease of the velocity field in the solid region, b is a relatively low constant introduced to avoid division by zero and f_L is the liquid fraction function. This function is assumed, through a simple model, to vary linearly with temperature in the mushy zone as follows:

$$f_L = \begin{cases} 1 & \text{if } T > T_L \\ \dfrac{T-T_S}{T_L-T_S} & \text{if } T_S \leq T \leq T_L \\ 0 & \text{if } T < T_S \end{cases} \tag{20}$$

where T is the temperature, T_S and T_L are the solidus and liquidus temperatures of the workpiece material.

- *Friction*

The level set method averages the material properties at the interface. As a result, the density is higher than the reality in the gas near the wire. Having a higher density reduces the flow rates in the gas, and therefore the shear stresses on the wire surface are reduced. To compensate this defect due to the level set method, a volume force has been added. It is only present at the time of the pulses. So, in order to obtain realistic droplet detachment, it is necessary to add a friction force expressed as follows [28]:

$$\vec{F}_{friction} = \left(F_{friction} \times \delta(\phi) \times freq_{current}\right)e_{\vec{z}} \; at\; the\; wire/plasma\; interface\; where\; T > T_{melt} \tag{21}$$

$freq_{current}$ represents the same periodic function used for $\vec{F}_{mag}$ to represent the droplet detachment frequency, T_{melt} is the melting temperature, and $F_{friction}$ is an artificial surface force helping to detach the droplet.

2.6. Computational domain and boundary conditions

The Fig. 1 shows the geometry and the table 1 shows the corresponding boundary conditions used in the model.

	AB_0	**B_0B**	**BC**	**CD**
T	T = 300 K	T = 300 K	Eq. 26	Eq. 24 and 25
(u,v,p)	v_{wire}	Eq. 22	$p = p_0$	$\vec{v} = \vec{0}$
$(V,\vec{A})$	Eq. 23	$\vec{j}.\vec{n} = 0$ $\vec{A}\times\vec{n} = \vec{0}$	$\vec{j}.\vec{n} = 0$ $\vec{A}\times\vec{n} = \vec{0}$	$\vec{j}.\vec{n} = 0$ $\vec{A}\times\vec{n} = \vec{0}$
	DE	**EF**	**FG**	**GA**
T	Eq. 24 and 25	$\vec{q}.\vec{n} = 0$	$\vec{q}.\vec{n} = 0$	$\vec{q}.\vec{n} = 0$
(u,v,p)	$\vec{v} = \vec{0}$	$\vec{v}.\vec{n} = 0$	$\vec{v}.\vec{n} = 0$	$\vec{v}.\vec{n} = 0$

$(V, \vec{A})$	$V = 0\,V$	$\vec{j}.\vec{n} = 0$ $\vec{B} = \vec{0}$	$\vec{j}.\vec{n} = 0$ $\vec{B} = \vec{0}$	$\vec{j}.\vec{n} = 0$ $\vec{B} = \vec{0}$

Table 1 - Boundary conditions

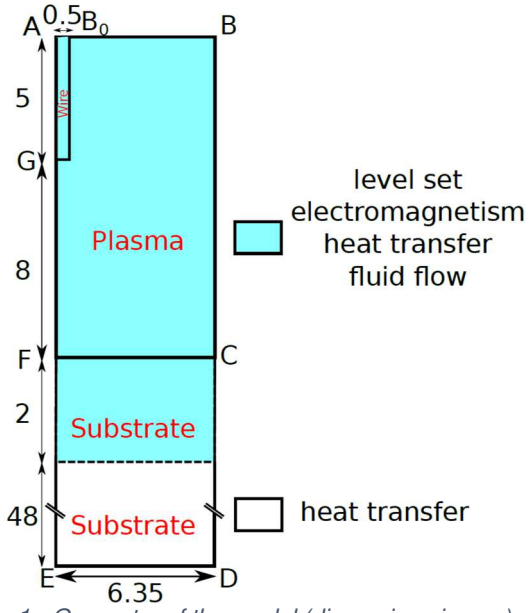

Fig. 1 - Geometry of the model (dimensions in mm)

The shielding gas flow rate is taken into account by imposing the value of the axial velocity field along the inlet boundary at the nozzle, according to the pipe flow equation [26]:

$$v_{gaz}(r) = \frac{2Q_m}{\rho\pi} \frac{\left[R_{nozzle}^2 - r^2 + \left(R_{nozzle}^2 - R_w^2\right)\frac{ln(r/R_{nozzle})}{ln(R_{nozzle}/R_w)}\right]}{\left[R_{nozzle}^4 - R_w^4 + \frac{(R_{nozzle}^2 - R_w^2)^2}{ln(R_{nozzle}/R_w)}\right]} \quad (22)$$

where $Q_m = \rho Q_v$ is the mass flow rate of argon shielding gas, Q_v is the volume flow rate of gas, R_{nozzle} is the nozzle internal radius and R_w is the radius of the filler wire.

Since it is difficult to measure the current density distribution along AB line (Fig. 1), a floating potential is specified in COMSOL Multiphysics®. The software calculates a constant voltage on this boundary such that the integration of the current density equals the imposed current. With such a boundary, the common profile of the current proposed in [18], [29] is obtained:

$$I = \int_{\partial\Omega} -\vec{n}.\vec{j}\, dS \quad (23)$$

Radiation and convection losses are applied to the surface of the substrate. The convection losses are calculated from:

$$q_c = -h_c(T - T_{amb}) \quad (24)$$

where h_c is a convective heat-transfer coefficient and T_{amb} is ambient temperature.

The radiation losses are determined from:

$$q_r = -\varepsilon\sigma_B\left(T^4 - T_{amb}^4\right) \quad (25)$$

where ε is the metal emissivity, σ_B is the Stefan-Boltzmann constant and T is the temperature at the metal surface.

For the open boundary of the plasma domain (BC line), the outflow condition of Comsol Multiphysics software is chosen, which is equivalent to an insulation condition:

$$\vec{q}.\vec{n} = 0 \quad (26)$$

The materials used are argon for shielding gas and 304 stainless steel for the substrate and the consumable electrode. The properties are given in Table 2.

	304 stainless steel	Argon
Thermal conductivity k (W.m^{-1}.K^{-1})	$k(T)$ [30]	0.08
Specific heat c_p (J.kg^{-1}.K^{-1})	$C_p(T)$ [30]	510
Density ρ (kg.m^{-3})	7000	1
Dynamic viscosity μ_f (Pa.s)	0.001	0.1
Electrical conductivity σ_e (S.m^{-1})	7.7×10^5 [31]	$\sigma_e(T)$ [32]
Magnetic permeability μ_0 (H.m^{-1})	$4\pi \times 10^{-7}$ [16]	
Liquidus temperature T_l (K)	1723 [33]	
Solidus temperature T_s (K)	1673 [33]	
Melting temperature T_{fusion} (K)	1700 [33]	
Net emission coefficient ε_N (W.m^{-3}.ster^{-1})		$\varepsilon_N(T)$ [18]
Surface tension coefficient γ (N.m^{-1})	1.6 [18]	
Anode work function ϕ_a (V)	4.65 [34]	
Cathode work function ϕ_c (V)	4.65 [34]	
Effective work function ϕ_e (V)	2.63 [34]	
Richardson's constant A_r (A.m^{-2}.K^{-2})	3×10^4 [34]	
Ionization potential V_i (V)	15.68 [34]	
Reinitialization speed γ_{ls} (m/s)	10 if $T > T_{fusion}$ if not 0.001	
Interface thickness ε_{ls} (μm)	90	

Table 2 – Material properties and parameters

2.7. Mesh

All the calculations have been obtained with a computational domain meshed using standard linear triangular elements. The maximum mesh size is set to 0.16 mm in the level set domain, and 4 mm in the other domains. Computations are performed within 38 hours on 8 cores (3.47GHz) and require around 10 GB RAM (DDR3). A fixed time step of 1.10^{-5}s is used during all the heating and a free time step during the cooling.

3. Results and discussion

3.1. Experimental data

The definition and validation of the model are based on experimental data obtained by the Institut des Matériaux Jean Rouxel (IMN) in Nantes in France. In arc processes, various modes of metal transfer exist depending on many operating variables such as arc current. Here, an inert gas process based on pulsed metal is chosen. During this process, one droplet per pulse is created at the tip of the electrode with a detachment frequency of 25 Hz ($freq_{current}$). The substrate is a cylinder of 0.5 inch (12.7 mm) diameter and 100 mm height composed of 304 stainless steel. The wire is also made of 304 stainless steel, its diameter is 1 mm with a wire feeding rate of 2.45 m / min. The argon flow rate is 15 L / min. The distance

between the nozzle and the cylindrical substrate is 12 mm. During experiments, a pulse current waveform at a frequency of 25 Hz is applied between the wire and the substrate with a peak current of around 350 A (I_{max}) and a background current of around 20 A ($I_{average}$) (Fig. 2). However, in our model, the pulse is not taken into account in the inlet current, but is accounted for in the electromagnetic force and drag force of the fluid flow problem. So, a constant current of 20 A is prescribed for the electric problem via the floating potential, as explained in section 2.6. This current is applied for 2.4 s, leading to the deposition of 60 droplets for the first layer. Then, the arc extinguishes and the melt pool solidifies. When the surface temperature reaches around 300 °C, measured by an infrared camera, a new layer is created. This process is repeated to build the rod with 17 layers, as shown in Fig. 3. Note that, during the initial stages of the process, the distance between the electrode and the deposited is around 4.2 mm. At the end of the material supply, the distance is only about 2.7 mm.

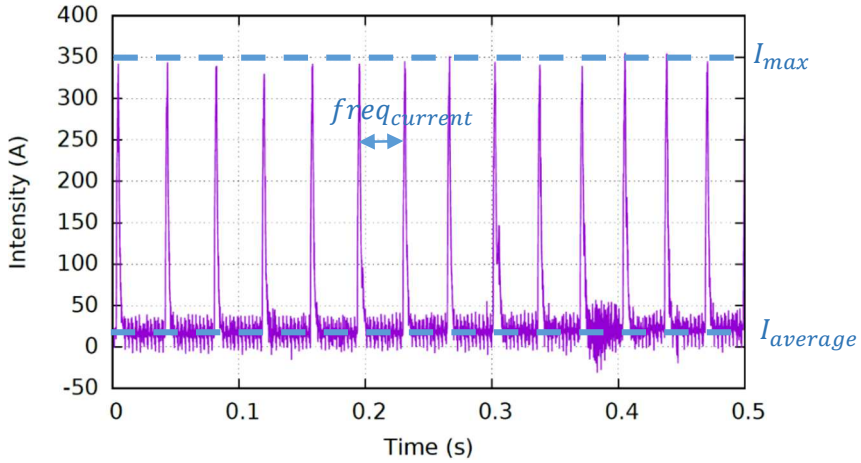

Fig. 2 – Measured electric current during the experiment

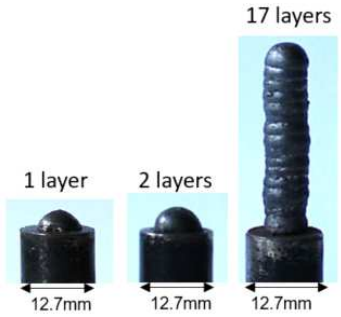

Fig. 3 - Photographies of different rods obtained with pulse WAAM

In order to validate the temperature calculated by the numerical model, several substrates were instrumented with three thermocouples (TC) of 50 µm diameter welded at the substrate surface (Fig. 4). The temperature measurements were carried out during the first two layers. An infrared camera was used to complete the temperature measurements. In addition, the final shape of the deposits was measured using a 3D scan to obtain the profile of the rod in different orientations for one and two layers. Macrographic cuts are also performed in order to analyse the fusion zone.

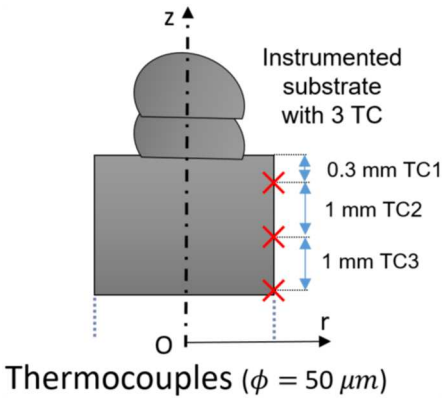

Fig. 4 - Diagram illustrating the positioning of the thermocouples

During the process, a high-speed camera was also used to measure the diameter and velocity of the droplets and to obtain the evolution of the geometry of the layers.

3.2. Simulation results

Using only the operating parameters, the model is able to simulate the different phenomena during WAAM process. Fig. 5 shows the temperature field in the arc plasma, the wire and the melt pool at different moments. The creation of the arc plasma is first observed. A maximum temperature of 12 800 K is obtained in the arc plasma with gas velocity of around 1.2 m/s. A melt pool is created at the electrode tip, that grows and reaches a diameter larger than the wire. At 0.04 s, a first pulse of current is set, that leads to the detachment of the droplet from the wire tip. During the flight of the droplet in the arc plasma, its temperature becomes homogeneous. For example, in Fig. 6, at t =1.206 s, the droplet has a lower temperature in its upper part (2441 K) than in its lower part (3154 K). While at t=1.218 s, the temperature in the droplet is homogeneous and is 2944 K. When the droplet reaches the top surface of the substrate, it induces the local melting of the substrate and the formation of a melt pool with a width larger than the droplet. This melt pool continuously grows during the deposition of other droplets and then solidifies during the extinction of the arc at 2.4s. A cooling of 21.6 s is then simulated before the creation of a new layer. In the simulations, the droplets impinge onto the melt pool at an average velocity of 0.7 m/s, which is twice as low than the velocity measured by the high speed camera estimated at 1.45 m/s. The underestimation of the droplet velocity by the model can be attributed to the level set method that averages the material properties between gas and metal at the interface. Nevertheless, the calculated droplet velocities are quite consistent with published values [15], [35].

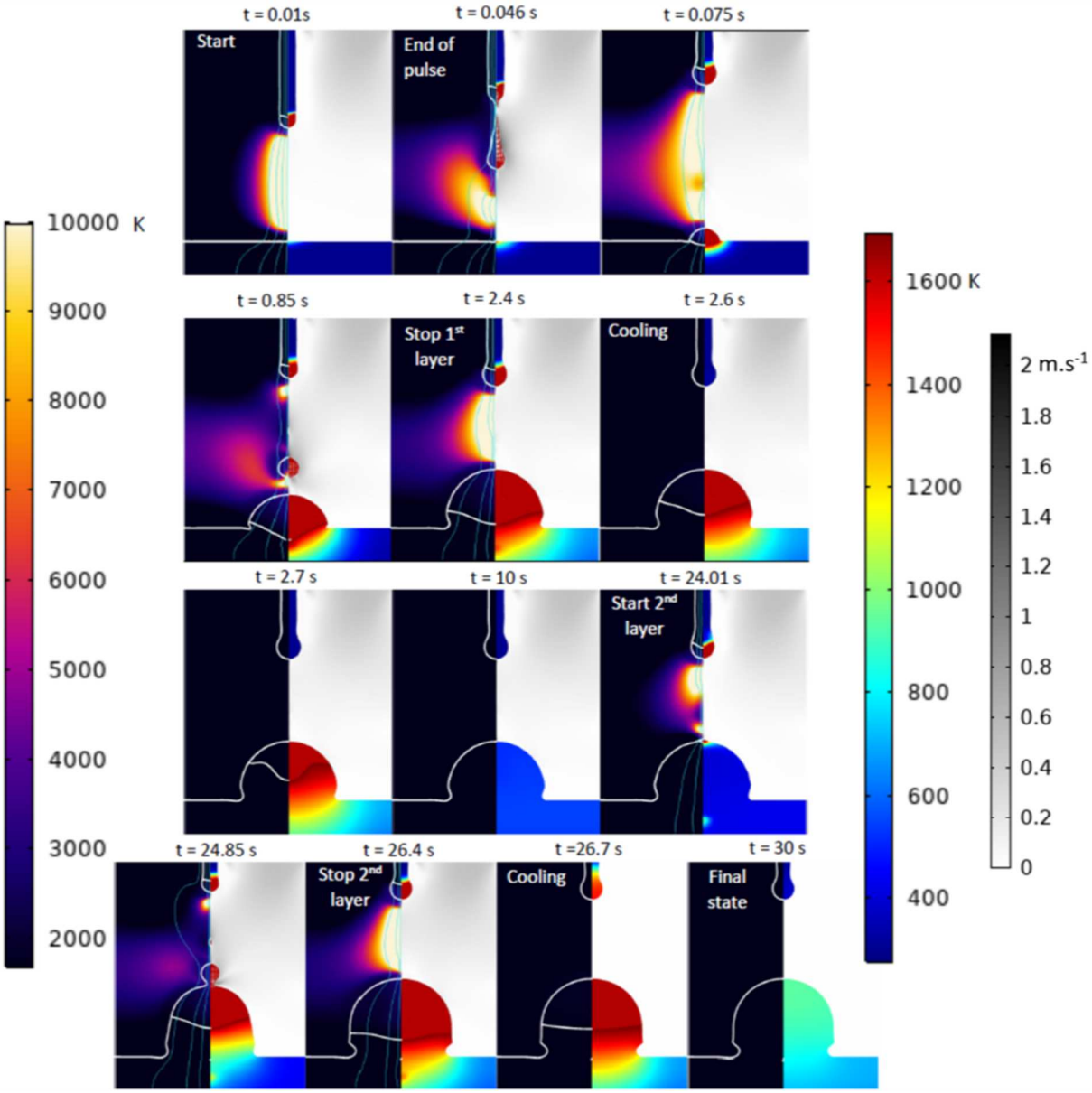

Fig. 5 – First two cycles of detachment of the droplet with the temperature field (in K) in the plasma with current density lines (on the left) and in the steel (on the right), the white line symbolizes the isothermal melting temperature

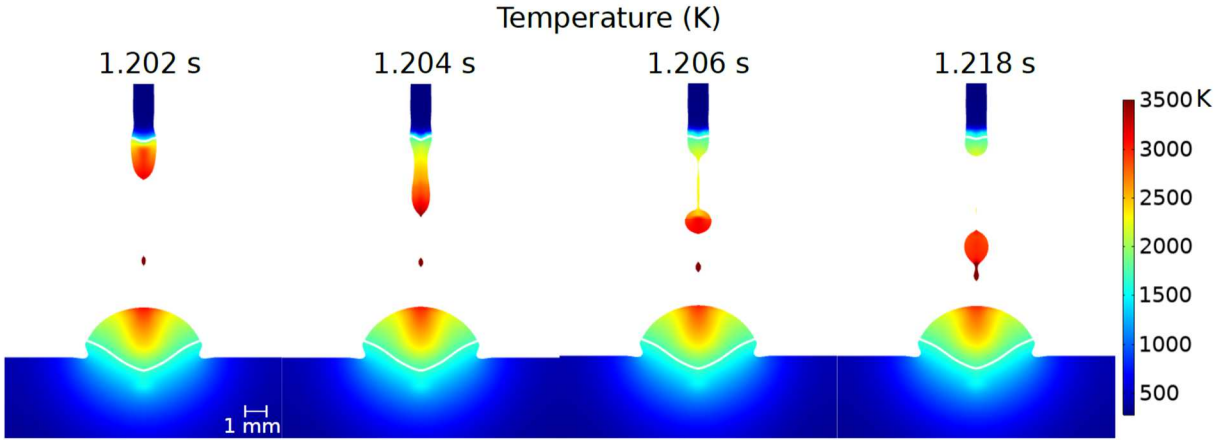

Fig. 6 - Distribution of temperature showing different moments during a pulse cycle (start at 1.2 s) with the white line symbolizing the isothermal melting temperature.

To further investigate the physical mechanisms during the creation of the droplet and its detachment, the magnitude of the driving forces (surface tension, electromagnetic force) is analysed in Fig. 7.

The electromagnetic forces are in the order of 9×10^4 N/m^3 while the forces related to the surface tension are in the order of 2×10^7 N/m^3. Therefore, the driving forces before the intensity pulse are those related to the surface tension, which keep the droplet at the electrode. However, during the pulse, electromagnetic forces contribute to the flattening of the droplet. This leads to an increase in surface tension along the liquid bridge. One explanation is that the material properties are averaged at the interface with the level set method, hence the use of an artificial force during the pulse is needed. This increase will create an acceleration of the flow in the droplet down and therefore, it will cause the elongation of the droplet until it is detached. During pulsation, the flow velocity within the droplet increases strongly from 0.25 m/s to 1.2 m/s. The speed has almost quintupled.

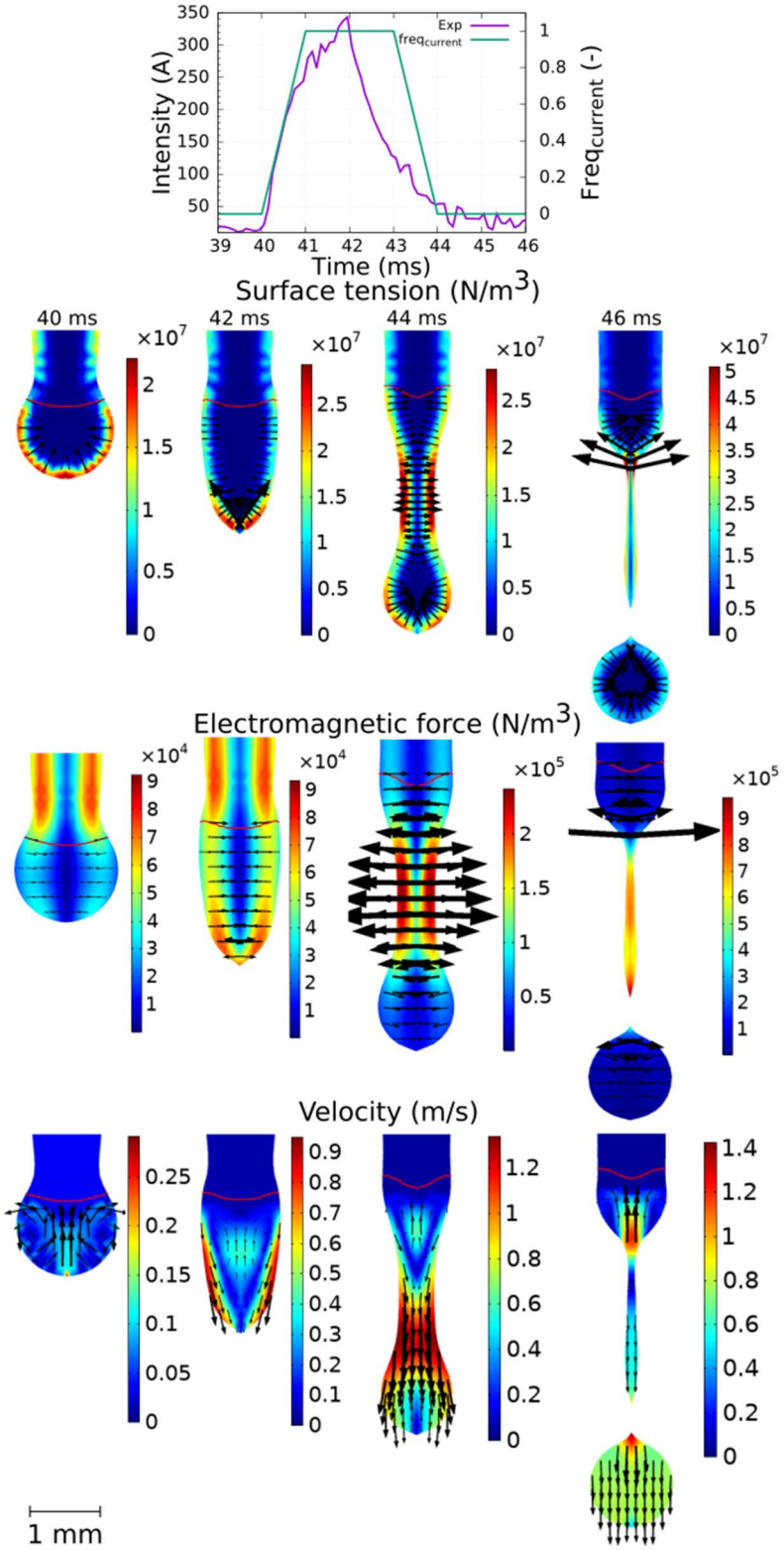

Fig. 7 - A sequence of the distribution of calculated process variables showing different moments during a pulse cycle

3.3. Droplets

From the operating parameters, it is possible to estimate the theoretical diameter of the droplets with this equation [11], based on mass conservation:

$$D_d = \left(6r_w^2 \frac{\rho_w}{\rho_d} \frac{v_w}{f_d}\right)^{1/3} \quad (27)$$

With the experimental parameter (v_w = 2.45 m/min, f_d = 25 Hz, r_w = 0.5 mm), the diameter of droplet is estimated at 1.35 mm. Moreover, with the high-speed camera, it is possible to check this value. With ImageJ software and the camera, the diameter droplet is estimated to 1.28 mm. From the model, the diameter of droplet can be estimated at 1.26 mm (Fig. 8). In relation to the camera, this represents an error of 1.5%.

In order to validate the good prediction of the model, the value of frequency has been changed from 25 Hz to 12.5 Hz. According to the equation (7), the theoretical diameter becomes 1.70 mm and the calculated diameter estimated with the model is 1.74 mm (Fig. 8). It represents a 2.35% error compared to the equation (27).

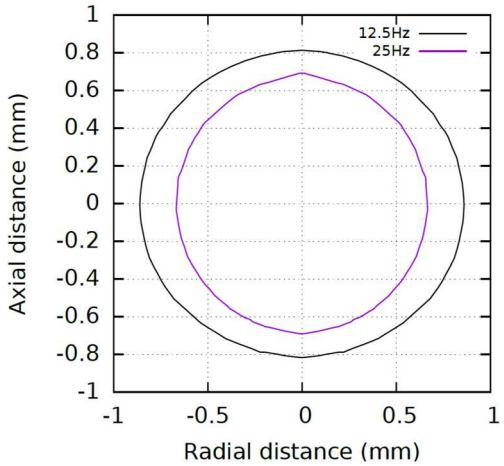

Fig. 8 - Diameter of droplet with frequencies at 25 Hz and 12.5 Hz

3.4. Deposit geometries for 1 layer and 2 layers

This model is able to predict the evolution of the melt pool sizes. Fig. 9 shows the evolution of the width and the height of the deposit for the first. It is interesting to note that the shape of the deposit undergoes three stages. At first, the evolution of the width and height are almost identical up to t = 0.8 s. At this point, the height of the deposit no longer changes while the width continues to increase up to 1 s. Then, the width of the deposit starts to stagnate while the height will only increase until the end of the process (t = 2.4 s). Fig. 9 does not show the oscillations related to droplet penetration. Indeed, the size of the melt pool is evaluated just before of the detachment of each droplet, at these different times the free surface is quite stabilized.

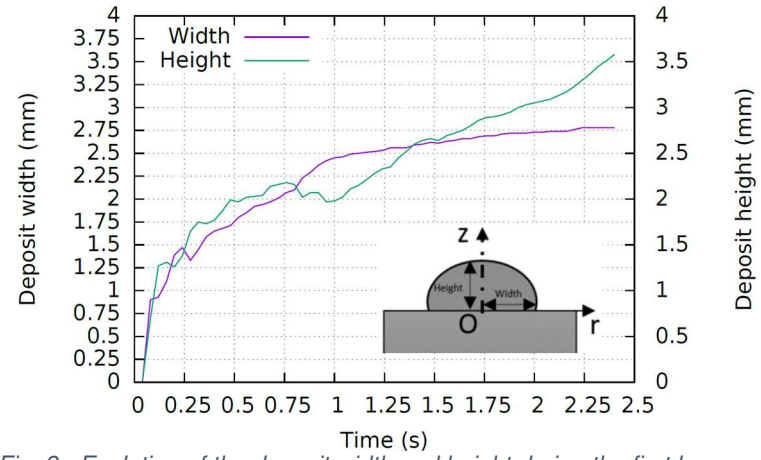

Fig. 9 - Evolution of the deposit width and height during the first layer

To better understand the influence of the droplet falling, the temperature and velocity fields in the melt pool at different moments during the impingement of one droplet are analysed in Fig. 10. In the melt pool, the main source of energy comes from droplets and not plasma. Indeed, when the droplet reaches the substrate surface, it induces a local increase of temperature. In the fusion bath, the main source of energy comes from droplets and not from plasma. Indeed, when the droplet reaches the surface of the substrate, it induces a local increase in temperature. Moreover, in the first moments, i.e. before the drop is detached, the substrate is not melted. It only melts on contact with the droplet. This same observation is made in the work of Hu and Tsai [10]. In addition, the impingement of droplet causes a fluid flow towards the bottom, advecting the heat downwards. This explains the deep penetration observed in the melt pool.

The surface tension, after the impact of the droplet, restores a spherical shape to the melt pool. Surface tension is the main driving force apart from the impact of droplet responsible for the outer shape of the deposit.

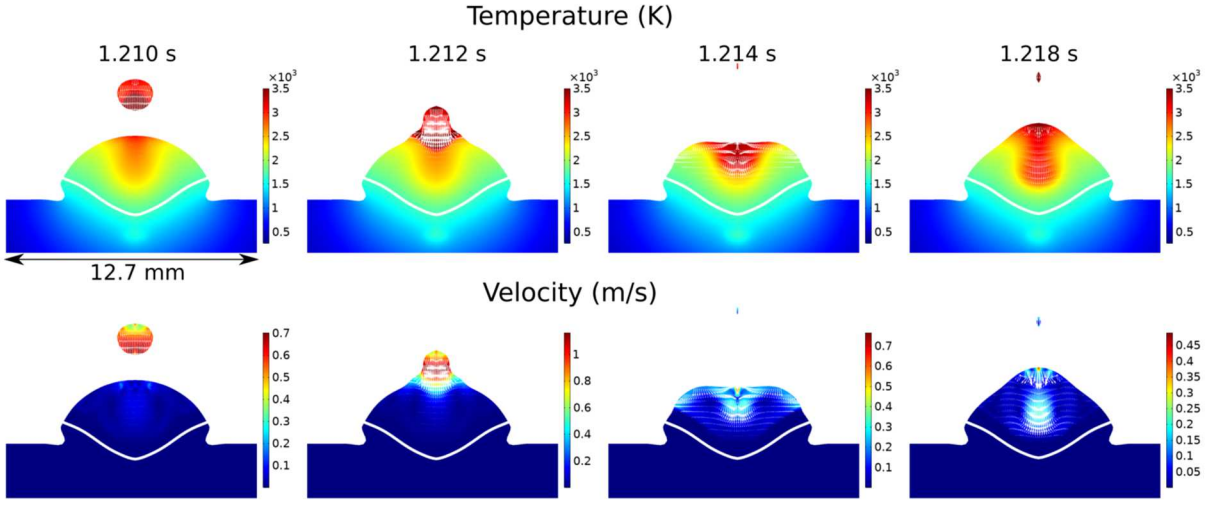

Fig. 10 - Flow velocity during the impact of a droplet

Using a 3D scan, and macrographic cuts, experimental profiles has been compared with those of the model.

The 3D scan allows to have profiles in different cutting planes. Four profiles have been selected, they vary by an angle of 45° along the vertical axis. The scan3D makes it possible to highlight the non-axisymmetry of the deposits (Fig. 11). The model predicts a geometry matching the profiles of the scan3D as well as the macrograph for one layer (Fig. 11a). The same observation is made for two layers (Fig. 11b). The calculated shapes are in good

agreement with the observed shapes of the layers. Thus, the model accurately predicts the mass addition induced by the melting of the wire. Moreover, the mass conservation in the model has been evaluated. For simulation with evolving interface tracked by the level set method, the conservation of mass is a challenge. To evaluate this mass conservation, the metal density has been integrated over the volume occupied by the phase having the variable ϕ comprised between 0.5 and 1 for t = 0 s and t = 56 s. This numerical mass is compared to the one given by the experimental mass flow rate. Here, the mass conservation is respected at 7% compared to the theoretical contribution for two layers.

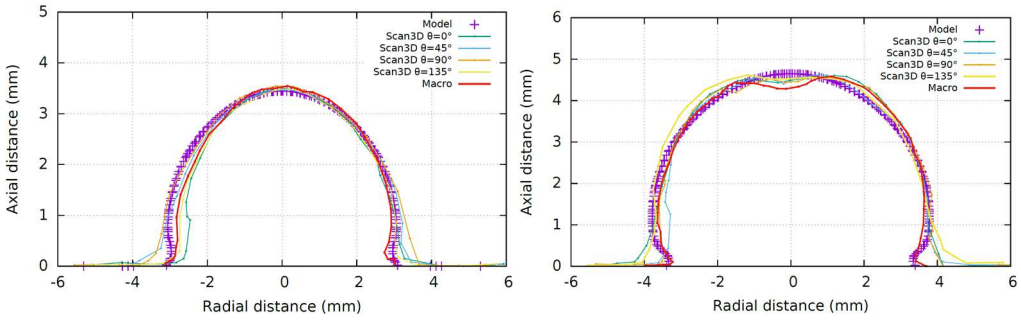

Fig. 11 - Comparisons of the profiles of the deposits from the model with those of the 3D scan and the macrographies for one layer (a) and two layers (b)

3.5. Comparisons between measured and calculated temperatures

The temperatures calculated by the model were compared with those measured by the thermal camera and the three thermocouples during the first two layers (Fig. 12). For TC2, and TC3, Fig. 12b-c shows a good agreement between the model, the thermocouple and the infrared camera for the first deposit and during its cooling. However, during the second deposit, only the material supply step (second temperature rise) is consistent with the thermocouple measurements as well as those of the camera. During cooling, the model cools faster than reality. One of the plausible explanations could come from not taking into account the contact resistances by the model. Indeed, Fig. 13 shows the presence of an air gap between the deposit and the substrate. Therefore, the deposit cannot evacuate the heat as quickly as in the model, since the model simulates a perfect contact between deposit and substrate, resulting in a faster cooling predicted by the model. For TC1, the model predicts temperatures that are too low, compared to experimental measurements for both deposits (Fig. 12a). One of the plausible reasons is that this thermocouple is more sensitive to the effects of the arc. However, the level set method tends to attenuate the flow in the arc and thus the heat transfer to the substrate, leading to lower temperatures.

In order to analyse the temperatures measured by the infrared camera, it is necessary to specify the value of the emissivity of the surface. After the WAAM experiments, this emissivity was estimated by comparing temperatures measured by two thermocouples welded at 0.3 mm and 2.5 mm from the top surface of the rod with infrared camera measurements. It was found an emissivity of 0.76 at 0.3 mm and 0.54 at 2.5 mm. Based on these measurements, the temperatures coming from the infrared camera have been calculated with an emissivity of 0.5 and 0.7 in Fig. 12.

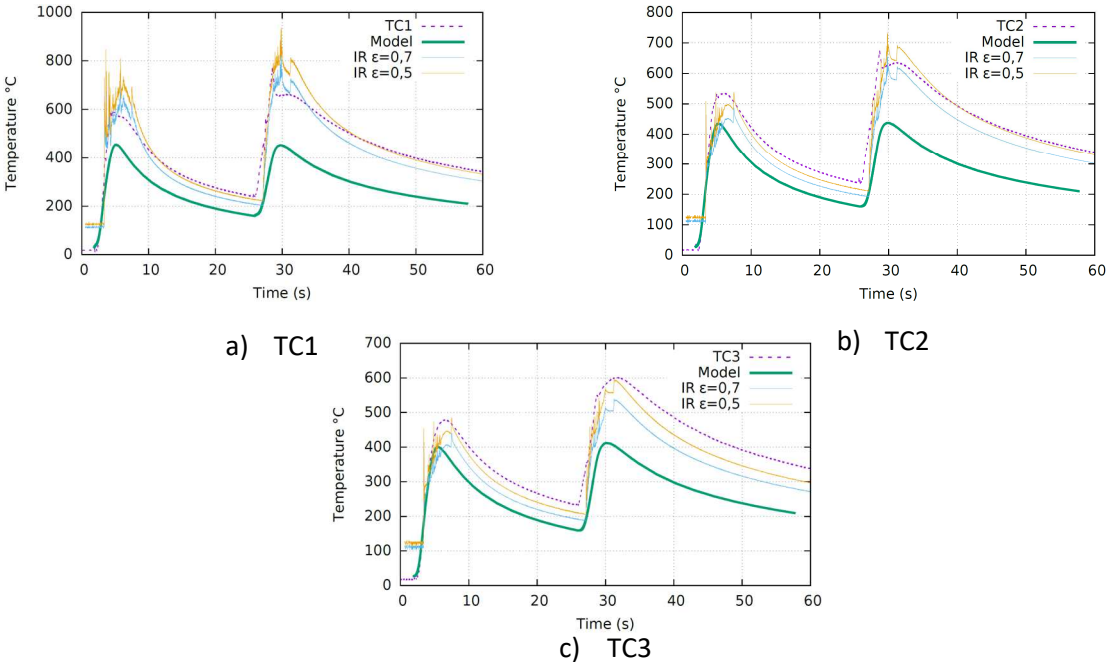

Fig. 12 - Comparisons of temperature measurements from the model with those of TC1 (a), TC2 (b), TC3 (c), and the infrared camera during the first two layers

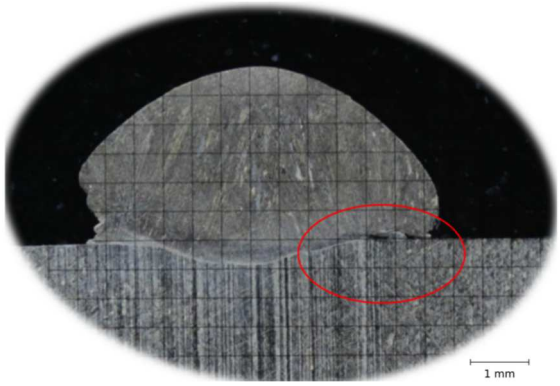

Fig. 13 – Macrograph illustrating the poor contact between the deposit and the substrate

4. Conclusions

In this study, heat transfer and fluid flow in the plasma and the melt pool were investigated through a transient 2D axisymmetric model to simulate a WAAM process. All the main driving phenomena are included in the model, which is based almost only on operating parameters and the numerical calibrations are reduced to the very minimum. The droplet generation, its transfer and impingement onto the melt pool as well as the melt pool dynamics were calculated. The model was used to simulate the first two layers of a vertical stainless steel rod. Each layer was composed of around sixty droplets. The model showed that the deposit width was mainly due to the falling of the first droplets, while the melt pool height increased continuously during the droplet falling. Moreover, the model also confirmed that, before the detachment of the droplet from the wire, the surface tension forces were dominant. However, during the pulse, the electromagnetic forces strongly increased along the liquid bridge, causing the droplet detachment. The simulation results exhibited good agreements with the thermocouples, macrographic cuts, 3D scans, infrared camera and high speed camera. The geometries of the deposits and the temperature of the built part were consistent with experimental data. Finally, a significant result of this work concerns the major role played by the droplet falling onto the melt pool. Its action strongly influences the melt

pool size, the fluid flow and the temperature field. Therefore, it appears essential to accurately model the interaction between droplets and melt pool in WAAM process.

This work will be extended to 3D configurations to simulate more complex geometries. Different WAAM processes could be simulated, based on pulse gas metal arc welding or cold metal transfer. Such model can also help to understand some defects and optimize the process parameter for different materials or geometries.

5. Acknowledgments

The authors are grateful to Pascal Paillard, Lauriane Guilmois and Paul Daheron from the Institut Matériaux Jean Rouxel (IMN – UMR 6502– Polytech Nantes, France) for their scientific and technical support during our experimental investigations.

6. References

[1] F. Martina and S. Williams, 'Wire+arc additive manufacturing vs. traditional machining from solid: a cost comparison', Apr. 2015.

[2] C. Cunningham, J. Flynn, A. Shokrani, V. Dhokia, and S. Newman, 'Invited Review Article: Strategies and Processes for High Quality Wire Arc Additive Manufacturing', *Addit. Manuf.*, vol. 22, pp. 672–686, Aug. 2018.

[3] A. Gomez Ortega, L. Corona Galvan, F. Deschaux-Beaume, B. Mezrag, and S. Rouquette, 'Effect of process parameters on the quality of aluminium alloy Al5Si deposits in wire and arc additive manufacturing using a cold metal transfer process', *Sci. Technol. Weld. Join.*, vol. 23, no. 4, pp. 316–332, Oct. 2017.

[4] X. Bai *et al.*, 'Numerical analysis of heat transfer and fluid flow in multilayer deposition of PAW-based wire and arc additive manufacturing', *Int. J. Heat Mass Transf.*, vol. 124, pp. 504–516, Sep. 2018.

[5] F. Hejripour, D. T. Valentine, and D. K. Aidun, 'Study of mass transport in cold wire deposition for Wire Arc Additive Manufacturing', *Int. J. Heat Mass Transf.*, vol. 125, pp. 471–484, Oct. 2018.

[6] L. A. Jones, T. W. Eagar, and J. H. Lang, 'A dynamic model of drops detaching from a gas metal arc welding electrode', *J. Phys. Appl. Phys.*, vol. 31, no. 1, pp. 107–123, Jan. 1998.

[7] L. A. Jones, T. W. Eagar, and J. H. Lang, 'Magnetic forces acting on molten drops in gas metal arc welding', *J. Phys. Appl. Phys.*, vol. 31, no. 1, pp. 93–106, Jan. 1998.

[8] H. G. Fan and R. Kovacevic, 'A unified model of transport phenomena in gas metal arc welding including electrode, arc plasma and molten pool', *J. Phys. Appl. Phys.*, vol. 37, no. 18, pp. 2531–2544, Sep. 2004.

[9] J. Hu and H. L. Tsai, 'Heat and mass transfer in gas metal arc welding. Part I: The arc', *Int. J. Heat Mass Transf.*, vol. 50, no. 5–6, pp. 833–846, Mar. 2007.

[10] J. Hu and H. L. Tsai, 'Heat and mass transfer in gas metal arc welding. Part II: The metal', *Int. J. Heat Mass Transf.*, vol. 50, no. 5–6, pp. 808–820, Mar. 2007.

[11] A. B. Murphy, 'Influence of droplets in gas–metal arc welding: new modelling approach, and application to welding of aluminium', *Sci. Technol. Weld. Join.*, vol. 18, no. 1, pp. 32–37, Jan. 2013.

[12] Y. Ogino and Y. Hirata, 'Numerical simulation of metal transfer in argon gas-shielded GMAW', *Weld. World*, vol. 59, no. 4, pp. 465–473, Jul. 2015.

[13] Y. Ogino, Y. Hirata, and A. B. Murphy, 'Numerical simulation of GMAW process using Ar and an Ar–CO2 gas mixture', *Weld. World*, vol. 60, no. 2, pp. 345–353, Mar. 2016.

[14] Y. Ogino, Y. Hirata, and S. Asai, 'Numerical simulation of metal transfer in pulsed-MIG welding', *Weld. World*, vol. 61, no. 6, pp. 1289–1296, Nov. 2017.

[15] Y. Zhao and H. Chung, 'Numerical simulation of droplet transfer behavior in variable polarity gas metal arc welding', *Int. J. Heat Mass Transf.*, vol. 111, pp. 1129–1141, Aug. 2017.

[16] Y. Zhao and H. Chung, 'Numerical simulation of the transition of metal transfer from globular to spray mode in gas metal arc welding using phase field method', *J. Mater. Process. Technol.*, vol. 251, pp. 251–261, Jan. 2018.
[17] Y. Zhao and H. Chung, 'Influence of power source dynamics on metal and heat transfer behaviors in pulsed gas metal arc welding', *Int. J. Heat Mass Transf.*, vol. 121, pp. 887–899, Jun. 2018.
[18] F. Lago, J. J. Gonzalez, P. Freton, and A. Gleizes, 'A numerical modelling of an electric arc and its interaction with the anode: Part I. The two-dimensional model', *J. Phys. Appl. Phys.*, vol. 37, no. 6, pp. 883–897, Mar. 2004.
[19] J. Mougenot, J.-J. Gonzalez, P. Freton, and M. Masquère, 'Plasma–weld pool interaction in tungsten inert-gas configuration', *J. Phys. Appl. Phys.*, vol. 46, no. 13, p. 135206, Apr. 2013.
[20] A. B. Murphy, M. Tanaka, K. Yamamoto, S. Tashiro, J. J. Lowke, and K. Ostrikov, 'Modelling of arc welding: The importance of including the arc plasma in the computational domain', *Vacuum*, vol. 85, no. 5, pp. 579–584, Nov. 2010.
[21] S. Osher and J. A. Sethian, 'Fronts propagating with curvature-dependent speed: Algorithms based on Hamilton-Jacobi formulations', *J. Comput. Phys.*, vol. 79, no. 1, pp. 12–49, Nov. 1988.
[22] E. Olsson and G. Kreiss, 'A conservative level set method for two phase flow', *J. Comput. Phys.*, vol. 210, no. 1, pp. 225–246, Nov. 2005.
[23] M. Khenner, A. Averbuch, M. Israeli, and M. Nathan, 'Numerical Simulation of Grain-Boundary Grooving by Level Set Method', *J. Comput. Phys.*, vol. 170, no. 2, pp. 764–784, Jul. 2001.
[24] L. T. Cheng and Y.-H. Tsai, 'Redistancing by flow of time dependent eikonal equation', *J. Comput. Phys.*, vol. 227, no. 8, pp. 4002–4017, Apr. 2008.
[25] M. Tanaka and J. J. Lowke, 'Predictions of weld pool profiles using plasma physics', *J. Phys. Appl. Phys.*, vol. 40, no. 1, pp. R1–R23, Jan. 2007.
[26] A. Traidia, 'Multiphysics modelling and numerical simulation of GTA weld pools', Ecole Polytechnique, 2011.
[27] B. Lafaurie, C. Nardone, R. Scardovelli, S. Zaleski, and G. Zanetti, 'Modelling Merging and Fragmentation in Multiphase Flows with SURFER', *J. Comput. Phys.*, vol. 113, no. 1, pp. 134–147, Jul. 1994.
[28] W.-I. Cho, S.-J. Na, C. Thomy, and F. Vollertsen, 'Numerical simulation of molten pool dynamics in high power disk laser welding', *J. Mater. Process. Technol.*, vol. 212, no. 1, pp. 262–275, Jan. 2012.
[29] K. C. Hsu, K. Etemadi, and E. Pfender, 'Study of the free-burning high-intensity argon arc', *J. Appl. Phys.*, vol. 54, no. 3, pp. 1293–1301, Mar. 1983.
[30] C. S. Kim, 'Thermophysical Properties of Stainless Steels', *Argonne Natl. Lab Ill USA*, no. ANL--75-55, 1975.
[31] C. Y. Ho and T. K. Chu, 'Electrical Resistivity and Thermal Conductivity of Nine Selected AISI stainless Steels', Thermophysical and Electronic Properties Information Analysis Center, CINDAS/Purdue Univ. 2595 Yeager Road, W. Lafayette, IN 47906, CINDAS-45, Sep. 1977.
[32] M. I. Boulos, P. Fauchais, and E. Pfender, *Thermal Plasmas*. Boston, MA: Springer US, 1994.
[33] H. G. Fan, H. L. Tsai, and S.-J. Na, 'Heat transfer and fluid flow in a partially or fully penetrated weld pool in gas tungsten arc welding', *Int. J. Heat Mass Transf.*, vol. 44, pp. 417–428, Aug. 2000.
[34] M. Tanaka, H. Terasaki, M. Ushio, and J. J. Lowke, 'A unified numerical modeling of stationary tungsten-inert-gas welding process', *Metall. Mater. Trans. A*, vol. 33, no. 7, pp. 2043–2052, 2002.
[35] J. Chapuis, E. Romero, F. Soulié, C. Bordreuil, and G. Fras, 'Transient behaviour of deposition of liquid metal droplets on a solid substrate', *Heat Mass Transf.*, vol. 52, no. 10, pp. 2283–2292, 2016.